Journal of Hazardous Materials 488 (2025) 137380

Contents lists available at ScienceDirect

Journal of Hazardous Materials

journal homepage: www.elsevier.com/locate/jhazmat

Ferrous iron oxidation in the presence of antimonate at neutral pH: Mutual effects on iron mineral products and antimony sequestration

L. Wegner [a,*], E.D. Burton [b], C. McCammon [c], A.C. Scheinost [d,e], B. Planer-Friedrich [f,1], S. Peiffer [a], K. Hockmann [g]

[a] University of Bayreuth, Bayreuth Center of Ecology and Environmental Research (BayCEER), Department of Hydrology, Bayreuth 95440, Germany
[b] Southern Cross University, Faculty of Science & Engineering, Lismore, NSW 2480, Australia
[c] University of Bayreuth, Bayerisches Geoinstitut, Bayreuth 95440, Germany
[d] The Rossendorf Beamline, European Synchrotron Radiation Facility, Grenoble 38043, France
[e] Helmholtz Zentrum Dresden Rossendorf, Institute for Resource Ecology, Dresden 01328, Germany
[f] University of Bayreuth, Bayreuth Center of Ecology and Environmental Research (BayCEER), Environmental Geochemistry, Bayreuth 95440, Germany
[g] University of Freiburg, Institute of Earth and Environmental Sciences, Applied Geochemistry, Freiburg 79104, Germany

HIGHLIGHTS

- Neutral pH Fe(II) oxidation at low molar Sb(V):Fe ratios produced lepidocrocite.
- A molar Sb(V):Fe ratio greater than 0.1 induced feroxyhyte formation.
- Sb(V) was incorporated into Fe oxides via Sb(V)-for-Fe(III) substitution.
- Sb(V) incorporation reached up to 16.2 mol% in the Fe(III) precipitates.

GRAPHICAL ABSTRACT

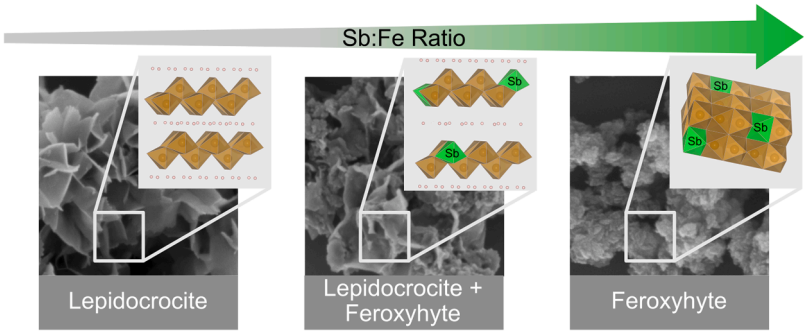

ARTICLE INFO

Keywords:
EXAFS
Feroxyhyte
Lepidocrocite
Mössbauer spectroscopy
Sb

ABSTRACT

Antimony is a priority pollutant, whose mobility in redox-dynamic environments may be controlled by interactions with Fe(III) hydroxide minerals that form via Fe(II) oxidation. In this study, we examined the Fe(III) hydroxide precipitates and associated mechanisms of Sb(V) sequestration that result from Fe(II) oxidation in the presence of Sb(V) under neutral pH conditions. To achieve this aim, oxidation experiments were carried out in O_2-saturated, Fe(II)-bearing solutions (buffered at pH 7) over a range of environmentally relevant Sb(V) concentrations (equivalent to Sb(V):Fe(II) molar ratios of 0, 0.01, 0.04, 0.1 and 0.25). Under these experimental conditions, Fe(II) oxidation occurred rapidly (within 20 minutes) causing associated removal of Sb(V) from solution via coprecipitation with the resulting Fe(III) hydroxides. At low Sb(V):Fe(II) ratios (< 0.1), lepidocrocite was the only Fe(III) mineral product of Fe(II) oxidation, whereas higher ratios resulted in formation of feroxyhyte. Both lepidocrocite and feroxyhyte retained Sb(V) within their crystal structure via Sb(V)-for-Fe(III) substitution. This mechanism of Sb(V) retention largely protected the solid-phase Sb(V) from release

* Corresponding author.
E-mail address: Laura.Wegner@uni-bayreuth.de (L. Wegner).
[1] We acknowledge with respect the involvement of Britta Planer-Friedrich, who sadly passed away during the submission of this manuscript.

https://doi.org/10.1016/j.jhazmat.2025.137380
Received 16 November 2024; Received in revised form 15 January 2025; Accepted 24 January 2025
Available online 26 January 2025

processes. Collectively, these results highlight the coupled role that interactions between Sb geochemistry and the Earth's near-surface Fe cycle can play in controlling both Fe(III) hydroxide mineralogy and Sb mobility.

1. Introduction

Antimony (Sb) is a suspected carcinogen that is listed as a priority pollutant by the US Environmental Protection Agency and the United Nations [55,56]. Despite its potentially hazardous nature, Sb is used in numerous products in our daily lives, including plastics, batteries, and glassware [16]. Antimony also plays an important role in a wide range of emerging green technologies, such as next-generation batteries for electric transport [35,4] or catalytic converters for the production of fuels and other value-added products from greenhouse gasses [26,36,53].

Due to rapid growth in industrial use of Sb, the global mine production of Sb has approximately tripled in the past 30 years [54]. This has resulted in a steadily growing legacy of environmental Sb contamination, which is often associated with an uncontrolled release of Sb into aquatic ecosystems. For example, Sb concentrations in surface and groundwater as high as 10's to 100's of mg L^{-1} have been reported in the vicinity of mining and ore-processing sites in Europe [19], North America [46], Asia [17], and Australia [2]. In contrast, natural Sb background concentrations typically do not exceed a few μg L^{-1} [14].

In natural waters, Sb occurs mainly in the +III and +V redox states, with Sb(V), speciating mainly as $Sb(OH)_6^-$ in the absence of complexing agents, being predominant under oxic to slightly reducing conditions [8,15,20,38,41]. The environmental behavior of Sb(V) is strongly influenced by interactions with Fe(III) hydroxides (a term used here to collectively refer to Fe(III) oxides, hydroxides, and oxyhydroxides) [33,38,50,6]. Oxidation of soluble aqueous Fe(II) to poorly soluble Fe(III) is a well-known pathway for the formation of Fe(III) hydroxide minerals [11]. This pathway commonly occurs in situations where anoxic Fe(II)-bearing water is exposed to oxic conditions, such as during discharge of subsurface water from underground mine workings to well-oxygenated surface zones [10,9]. A recent study showed that in such solutions, Sb(III) and Fe(II) can be co-oxidized to Sb(V) and Fe(III), respectively [60].

Despite the clear environmental relevance of such situations, the behavior of Sb(V) during the initial Fe(III) hydroxide formation via aqueous Fe(II) oxidation has received surprisingly little attention. Results from incubation experiments with contaminated soil indicate that Sb(V) may be removed from the aqueous phase upon Fe(II) oxidation [22,38]; presumably via Sb(V) uptake by newly-formed Fe(III) hydroxides. In addition, recent research on the formation of schwertmannite (a sulfate-bearing Fe(III) hydroxide) via aqueous Fe(II) oxidation under strongly acidic pH conditions has revealed that Sb(V) itself can affect the final Fe(III) hydroxide mineralogy, with high Sb(V) concentrations acting, for example, to inhibit schwertmannite formation [47]. However, at present, the effect of Sb(V) in potentially shaping the mineralogy of Fe(III) hydroxides that are produced via Fe(II) oxidation under near-neutral pH remains largely unexplored. Likewise, the mechanisms that control Sb(V) uptake by Fe(III) hydroxides that are formed via Fe(II) oxidation under such conditions have not been systematically explored. This represents a significant knowledge gap, especially considering that Fe(III) hydroxide precipitation in the presence of Sb(III) has previously been found to lead to substantial Sb immobilization [59].

The aim of this study was to examine the Fe(III) hydroxide mineral products and associated mechanisms of Sb(V) sequestration that result from Fe(II) oxidation in the presence of Sb(V) under near-neutral pH conditions. To achieve this aim, experiments were carried out in oxygen-saturated Fe(II)-bearing solutions that contained a range of environmentally relevant Sb(V) concentrations (equivalent to initial aqueous Sb(V):Fe(II) molar ratios of 0, 0.01, 0.04, 0.1 and 0.25). The oxidation experiments were buffered at pH 7, as Sb-contaminated mining waters are often buffered at near-neutral pH, due to the presence of abundant carbonate minerals [13,42]. After Fe(II) oxidation was complete, samples of the resulting Fe(III) hydroxides were characterized using X-ray diffractometry (XRD), transmission electron microscopy (TEM), scanning electron microscopy (SEM), Mössbauer spectroscopy, extended X-ray absorption fine structure (EXAFS) spectroscopy and wet chemical extraction techniques.

2. Methods

2.1. General methods

All glassware was soaked in 2 % HCl overnight and rinsed with ultrapure water (MilliQ) three times prior to use. All reagents were analytical grade. Solutions were prepared using MilliQ water. An ambient temperature of 21 ± 1 °C was maintained for all reactions.

2.2. Fe(II) oxidation experiment

For the Fe(II) oxidation experiment, four treatments with molar Sb:Fe ratios of 0.01, 0.04, 0.10, and 0.25 (treatments Sb-0.01, Sb-0.04, Sb-0.1, and Sb-0.25), as well as an Sb-free control treatment (Sb-0), were prepared in triplicate. These Sb:Fe ratios were prepared in 4 L of a background electrolyte solution containing 100 mmol L^{-1} KCl, with 50 mmol L^{-1} 3-(N-morpholino)-propane sulfonic acid (MOPS) as a pH buffer (adjusted to pH 7 using 6 M KOH). It should be noted that sulfonate-containing buffers, such as MOPS, have been widely used in previous studies of Sb and Fe behaviour [21,23,24,7,8], and have been shown to have no significant interaction with metal ions in solution due to steric reasons [12,28]. Aliquots of a 10 mmol L^{-1} Sb(V) stock solution, prepared from $KSb(OH)_6$, were added to achieve aqueous Sb(V) concentrations of 0.01, 0.04, 0.10, or 0.25 mmol L^{-1}. The Sb concentrations were chosen to represent concentrations frequently found in the vicinity of mining sites [17,3]. The oxygen supply was provided by stirring the solution vigorously on a magnetic stirrer at 1500 rpm and bubbling ambient air through it using an air pump.

The Fe(II) oxidation reaction was initiated by adding 1 mmol L^{-1} $FeCl_2$ dissolved in 0.01 M HCl to the aerated solution. 10 mL subsamples were collected from the solution with a syringe immediately before the start of the experiment, as well as at defined intervals (2, 4, 6, 8, 10, 15, 20, 25, 30, 40, 50, and 60 minutes) following the addition of the Fe(II) solution. The samples were passed through 0.2 μm cellulose acetate filters (Minisart NML, Sartorius), stabilized with 200 μL concentrated HCl, and stored in a refrigerator. After the last sampling, the precipitates were allowed to settle for 1 hour and then separated from the liquid by repeated centrifugation and decantation (4 min at 4000 rpm each). Since remains of the electrolyte solution had been shown to cause interferences in the XRD patterns, the background electrolyte was removed by washing with methanol [8]. The precipitates were stored at −80 °C until they were freeze-dried (Alpha 1–4 LDplus, Christ) and ground for solid-phase analyses.

2.3. Analyses

The pH and dissolved oxygen concentrations were monitored with a HACH 40D multi-Meter equipped with a luminescent dissolved oxygen probe (IntelliCAL LDO101, Hach) and a gel-filled pH electrode (IntelliCAL PHC101, Hach). This data can be found in the Supporting Information (SI Figure S1).

Dissolved Fe(II) concentrations in the stabilized samples were measured photometrically using the phenanthroline method [1] within

1 h after the experiment. The detection limit (DL), determined as the mean of 3 replicates + 3 * standard deviation, was 1 mg L^{-1}. Determination of total Sb and Fe concentrations in stabilized aqueous samples and extracts was conducted by inductively coupled plasma mass spectroscopy (ICP-MS, Perkin-Elmer, ELAN-DRCe, DL: 0.005 mg L^{-1}).

X-ray diffractometric analyses were conducted using a Bruker D4 Endeavor instrument with a Co X-ray source (λ = 0.178890 nm), scanning from 5 to 90 °2θ with a 0.02 °2θ step-size and a 2 s count-time, with powder samples mounted on sample holders using ethanol. For transmission electron microscopy (TEM), a Hitachi HF5000 Cs-STEM/TEM instrument operated at 200 kV was used for imaging. For selected area electron diffraction (SAED), a Gatan Digital Micrograph was employed to acquire images on a Gatan Oneview camera in 4kx4k pixel collection mode. The sums of four patterns per treatment were collected to increase result quality. Scanning electron microscopy samples (SEM) were mounted on Si wafers, coated with platinum, and analyzed using a Zeiss Ultra plus instrument with an Inlens SE-Detector (Everhart Thornley).

^{57}Mössbauer spectra of solid-phase samples and synthetic feroxyhyte (δ′-FeOOH, synthesized according to [51]) were obtained in transmission mode on a constant-acceleration Mössbauer spectrometer equipped with a nominal 1.85 GBq ^{57}Co/Rh γ-radiation source. The velocity scale was calibrated relative to a 25 μm thick α-Fe foil at room temperature. Dried powders (~55 mg) were loaded into plastic sample holders (1.13 cm^2) and placed in a continuous-flow cryostat with the sample in N_2 vapor for measurement at 80 K, whereas the ^{57}Co/Rh source remained at room temperature. Spectra were analyzed using the Recoil [32] and MossA software [44] by applying Voigt-based fitting routines.

X-ray Absorption Near-Edge Structure (XANES) and Extended X-ray Absorption Fine-Structure (EXAFS) spectra were acquired at the Rossendorf Beamline (BM20) at the European Synchrotron Radiation Facility (ESRF), Grenoble, France [49]. XANES and EXAFS spectra were collected at the Sb K-edge (30,491 eV) in transmission mode. The energy of the liquid N_2-cooled Si(111) double-crystal monochromator (DCM) was calibrated using an Sb foil. During the measurement, the samples were kept at 15 K with a closed-cycle He cryostat (CryoVac) to avoid photon-induced changes of oxidation state and to reduce thermal disorder [31]. Least-square shell-fit analysis of Sb K-edge EXAFS spectra was performed in Artemis [48], as described previously [7]. Details on the data collection and processing are available in SI Section 2. Wavelet transform (WT) analysis was used to resolve the centres of the backscattering wave functions in both *k*-space ($Å^{-1}$) and *R*-space (Å), thus offering additional information to discriminate different atoms within one atomic shell, which cannot be identified by shell-by-shell fitting [18].

The total Sb concentration in the precipitates was determined by digesting 50 mg of freeze-dried precipitates in 6 M HCl within 48 h [30]. The operationally-defined surface-bound fraction of Sb was assessed via a 1 M KH_2PO_4 extraction [29], and a repeated desorption experiment was used to examine the pool of easily remobilized Sb. Experimental details on the extraction experiments and their effectiveness are given in SI Section 3. The percentage of Sb(V)-for-Fe(III) substitution was calculated from the extraction assay using SI Equation 1.

3. Results and discussion

3.1. Trends in aqueous Fe and Sb concentrations

Aqueous Fe(II) was removed from solution in all treatments within approximately 20 min (Fig. 1). This occurred together with the formation of red-orange Fe(III) hydroxide particles and parallel decreases in aqueous Sb concentrations. These trends are consistent with the Sb uptake by Fe(III) hydroxide phase(s) that formed via Fe(II) oxidation. While almost all aqueous Sb was removed by such uptake in the Sb-0.01 treatment, approximately 20–30 % of the initial aqueous Sb remained in solution for the Sb-0.04, Sb-0.1 and Sb-0.25 treatments (SI Figure S4).

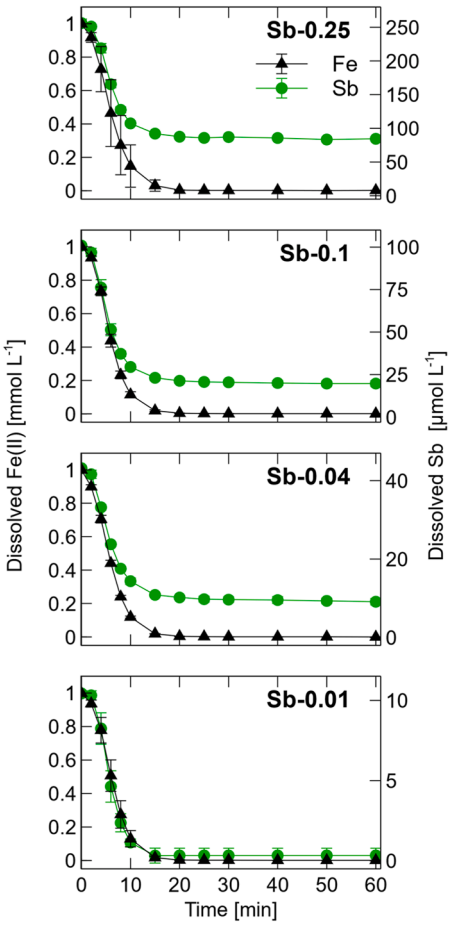

Fig. 1. Dissolved Fe(II) and Sb concentrations during Fe(II) oxidation at molar Sb:Fe ratios of 0.25, 0.1, 0.04, and 0.01. Error bars indicate the standard deviation of triplicates.

The final aqueous Sb concentrations at the completion of the oxidation experiment equate to solid-phase Sb concentrations in the Fe(III) hydroxide phases of approximately 75 ± 3, 225 ± 12, 547 ± 79 and 1400 ± 19 $mmol_{Sb}$ g_{Fe}^{-1} in the Sb-0.01, Sb-0.04, Sb-0.1 and Sb-0.25 treatments, respectively (Table 1).

3.2. Mineralogy and solid-phase Fe characterization

X-ray diffractometry revealed the presence of lepidocrocite (γ-FeOOH) and/or feroxyhyte in solids collected at the completion of the Fe(II) oxidation experiment. Specifically, in the Sb-0 treatment, all XRD peaks could be attributed to lepidocrocite (Fig. 2a), with SEM showing the presence of plate-like lepidocrocite crystals with sharp edges (Fig. 3a). In this treatment (Sb-0), lepidocrocite formation was expected,

Table 1
Characteristics of the solid-phase products after Fe(II) oxidation at molar Sb:Fe ratios of 0, 0.01, 0.04, 0.1, and 0.25 (denoted as Sb-0, Sb-0.01, Sb-0.04, Sb-0.1 and Sb-0.25, respectively). Fe(III) substitution was calculated from extraction data using Equation 1 in SI.

Treatment	Sb solid phase concentration (mmol g^{-1})	Fe(III) substitution (mol%)	d-spacing of (020) plane (Å)
Sb−0	< 0.2	0.0	6.3
Sb−0.01	75 ± 3	1.0	6.8
Sb−0.04	225 ± 12	3.4	8.3
Sb−0.1	547 ± 79	8.2	8.3
Sb−0.25	1400 ± 19	16.2	-

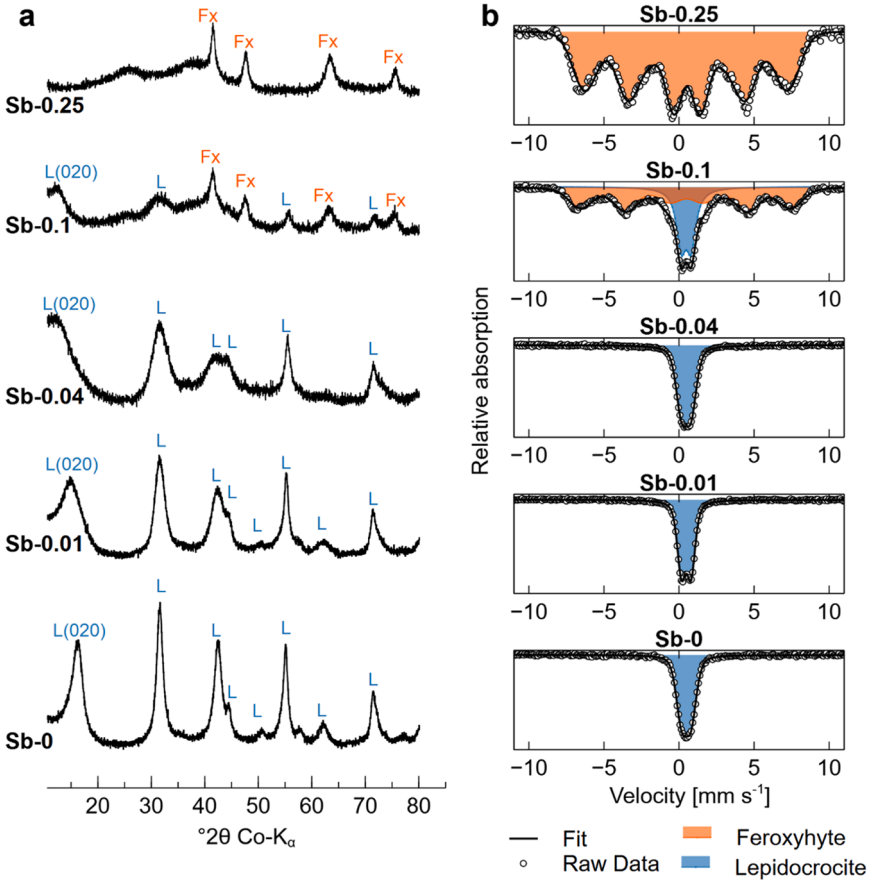

Fig. 2. a) X-ray powder diffractograms and (b) 80 K Mössbauer spectra of solid-phase products after Fe(II) oxidation at molar Sb:Fe ratios of 0, 0.01, 0.04, 0.1, and 0.25 (denoted as Sb-0, Sb-0.01, Sb-0.04, Sb-0.1 and Sb-0.25, respectively. In (a), the labels "L" and "Fx" denote lepidocrocite and feroxyhyte, respectively.

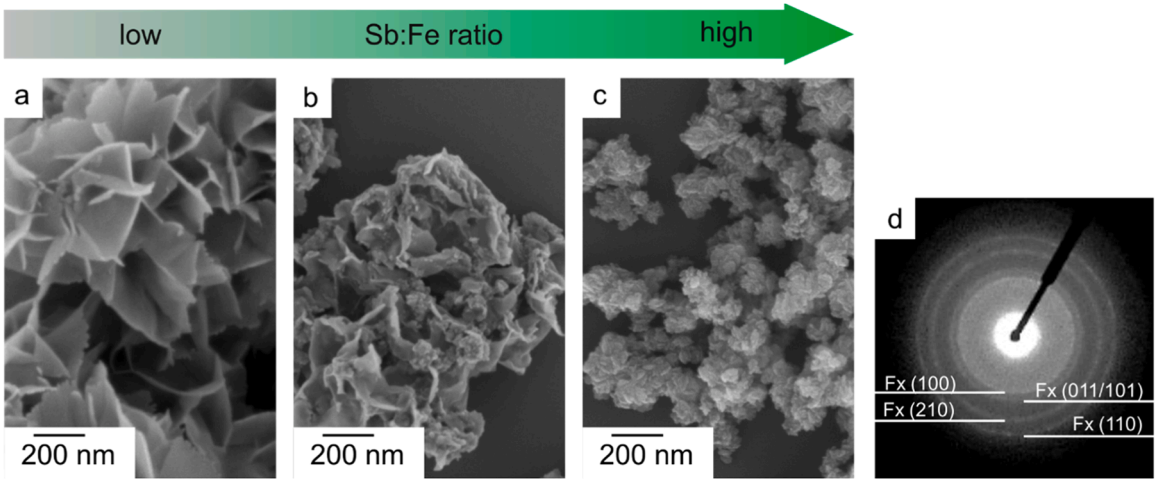

Fig. 3. Microscopic analyses of selected solid-phase products after Fe(II) oxidation: a) SEM image of lepidocrocite platelets formed at an Sb:Fe ratio of 0.01; b) SEM image showing the close association between distorted lepidocrocite platelets and feroxyhyte aggregates formed at an Sb:Fe ratio of 0.1; c) SEM image and d) corresponding TEM-SAED pattern of feroxyhyte aggregates precipitated an Sb:Fe ratio of 0.25. Additional TEM images of the other treatments are provided in the SI.

as lepidocrocite is well known to be the primary product of aqueous Fe (II) oxidation under similar circum-neutral pH conditions [34,52,60].

The XRD patterns indicate that lepidocrocite was the only mineral phase present in solids from the Sb-0.01 and Sb-0.04 treatments (Fig. 2a). However, in these treatments, an increase in lepidocrocite's XRD peak widths and a decrease in peak intensities was observed (relative to the Sb-0 treatment), with this effect being more pronounced for lepidocrocite which had formed at higher Sb concentrations. As such, the presence of Sb appears to have also caused a clear expansion along the lepidocrocite b-axis, which is evident from shifts in the position of the (020) peak in the XRD patterns for the Sb-0.01, Sb-0.04 and Sb-0.1 treatments relative to the Sb-0 treatment (Fig. 2a). This shift is associated with an increase in d-spacing from 6.3 Å to 8.3 Å (Table 1) in the lepidocrocite structure.

Table 2
80 K Mössbauer parameters of feroxyhyte (Fx), lepidocrocite (L) and the solid-phase products after Fe(II) oxidation at molar Sb:Fe ratios of 0, 0.01, 0.04, 0.1, and 0.25.

Sample	Species	CS (mm s^{-1})[a]	ΔE_Q or ε (mm s^{-1})[b]	B_{hf} (T)[c]	R.A.[d]
Feroxyhyte[e]	Fx	0.48 ± 0.01	−0.06 ± 0.01	46.4 ± 0.6	100 %
Lepidocrocite[f]	L	0.49 ± 0.05	0.65 ± 0.05	-	100 %
Sb−0	L	0.49 ± 0.01	0.64 ± 0.01	-	100 %
Sb−0.01	L	0.48 ± 0.01	0.64 ± 0.01	-	100 %
Sb−0.04	L	0.48 ± 0.01	0.65 ± 0.01	-	100 %
Sb−0.1	L	0.48 ± 0.01	0.66 ± 0.01	-	33 ± 2 %
	Fx	0.48 ± 0.02	−0.04 ± 0.01	43.5 ± 0.1	67 ± 2 %
Sb−0.25	Fx	0.51 ± 0.01	−0.03 ± 0.01	33.1 ± 0.5	100 %

[a]Center shift (relative to α-Fe^0). [b]Quadrupole splitting (paramagnetic) or quadrupole shift (magnetic). [c]Hyperfine magnetic field. [d]Relative abundance. [e] Synthesized according to Schwertmann and Cornell [51] and verified via XRD; [f]According to previously published values [25].

In contrast, solids from the Sb-0.1 treatment display additional XRD peaks at 41.5, 47.5, 63.4, and 75.4 °2θ, while the intensities of the XRD peaks of lepidocrocite further decreased (Fig. 2a). The positions of these XRD peaks matched those previously reported for feroxyhyte [43]. At even higher Sb concentrations, i.e. in the Sb-0.25 treatment, feroxyhyte was the only mineral product that was detectable via XRD. Transmission electron microscopy with SAED confirmed feroxyhyte to be the only mineral phase present in solids from the Sb-0.25 treatment (Fig. 3c and d, SI Figure S5). Examination via SEM revealed that feroxyhyte in the Sb-0.25 treatment existed as very fine crystallites that were aggregated into nanometer-scale cloud-like clusters (Fig. 3c). Feroxyhyte is a rare short-range order FeOOH polymorph that occurs in a range of environmental settings, including those characterized by rapid Fe(II) oxidation [11,5,58,57].

^{57}Fe Mössbauer spectra of precipitates collected at 80 K from the Sb-0, Sb-0.01, and Sb-0.04 treatments exhibited a paramagnetic doublet with hyperfine values that are consistent with lepidocrocite (Fig. 2b, Table 2) [25]. Precipitates from the Sb-0.1 treatment presented as a sextet (67 % of the total spectral area), in addition to the lepidocrocite doublet (33 % of the total spectral area), while in the Sb-0.25 treatment, the Mössbauer spectrum consisted solely of a sextet. Fitting of the hyperfine values for the sextets revealed center shift (CS) and quadrupole splitting (ΔEQ) values that are similar to synthetic feroxyhyte (Table 2, and SI Figure S6, S7).

The ^{57}Fe Mössbauer spectroscopy results show that the magnetic hyperfine field (Bhf) for feroxyhyte that formed during the Fe(II) oxidation experiment were reduced relative to the Bhf of pure feroxyhyte. Decreases in the BhF value can be caused by the substitution of diamagnetic ions into the Fe(III) hydroxide crystal structure [40]. In the context of the present study, the Bhf decreases may therefore reflect substantial levels of substitution of Fe(III) by diamagnetic Sb in feroxyhyte. This suggests that the removal of Sb(V) from solution in the Sb-0.1 and Sb-0.25 likely involved a significant degree of Sb(V) coprecipitation with Fe(III) during feroxyhyte formation.

Collectively, the XRD, TEM, and Mössbauer spectroscopy results clearly show that aqueous Fe(II) oxidation in the presence of low levels of Sb(V) led to lepidocrocite formation, whereas Fe(II) oxidation in the presence of higher levels of Sb(V) instead led to feroxyhyte formation. Hence, it appears that Sb(V) acts as a mineral switch during near-neutral pH Fe(II) oxidation, shifting the mineralogy of the resulting Fe(III) hydroxide from lepidocrocite to feroxyhyte. To the best of our knowledge, the present study is the first to identify this effect of Sb(V) in steering the mineralogy of Fe(III) hydroxides that are produced via aeration of Fe(II)-bearing solutions. However, this finding echoes earlier research in anoxic systems on ferrihydrite transformation in the presence of Sb(V), which also found that high levels of Sb(V) promoted the formation of feroxyhyte [21,6,8]. Our results also concur with an earlier study in which feroxyhyte was found in Sb-rich sediments in the vicinity of an Sb mine [27].

3.3. Solid-phase Sb characterization

Linear combination fitting (LCF) of the Sb K-edge XANES spectra for solids collected from the oxidation experiment confirmed the presence of Sb(V) with negligible solid-phase Sb(III) (SI Figure S8). Modelling of the Sb K-edge EXAFS spectra revealed Sb coordination by a first shell comprising 4.6 – 6.7 O atoms at an inter-atomic distance of 1.98 Å (Fig. 4, Table 3). This is consistent with an octahedral coordination of Sb (V) by O, thereby supporting the results of our LCF analyses of the XANES spectra [50].

In the Sb-0.01 treatment, subsequent peaks in the Fourier transform were well described by Sb-Fe scattering paths at 3.13 Å and 4.03 Å with CNs of 4 and 1.6, respectively. Similar fitting results (Sb-Fe paths at 3.15 Å and 3.99 Å with CNs of 5.5 and 1.4, respectively) were found for the Sb-0.04 treatment (Table 3). Inter-atomic Sb-Fe distances of 3.13 Å and 4.03 Å are indicative of edge-sharing and single corner-sharing between adjacent SbO_6 and FeO_6 octahedra [37,39]. Linkages of this nature (with comparable CNs) are a defining feature of the local coordination environment around Fe atoms in lepidocrocite. This suggests

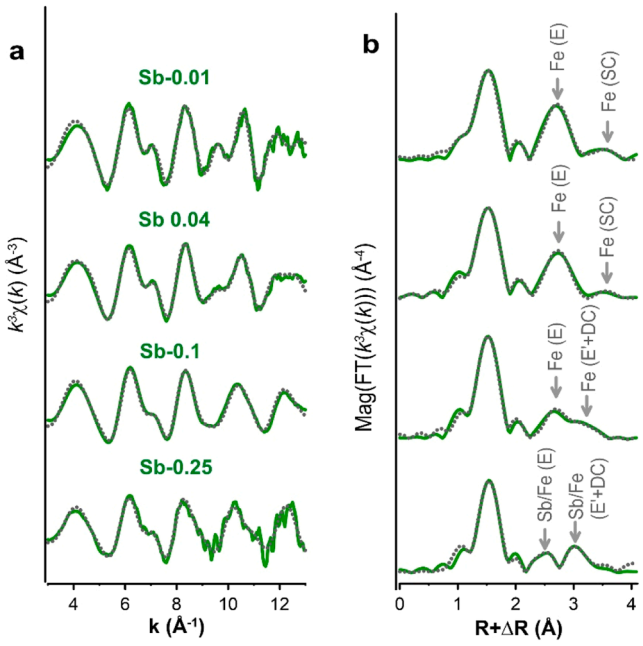

Fig. 4. (a) Sb K-edge EXAFS spectra and (b) Fourier-transform magnitudes of the Fe(III) hydroxide products formed at molar Sb:Fe ratios of 0.01, 0.4, 0.1, and 0.25 (denoted as Sb-0.01, Sb-0.04, Sb-0.1, and Sb-0.25, respectively). Solid lines represent experimental data and grey dotted lines are shell fits. Approximate positions of peaks in (b) due to the backscattering contributions of Sb and Fe in various coordination are indicated (DC = double-corner sharing; E = edge sharing within a single octahedral chain; E' = edge sharing between two octahedral chains; SC = single-corner sharing).

Table 3
Antimony K-edge EXAFS shell-fit results of the Fe oxide products at molar Sb:Fe ratios of 0.01, 0.4, 0.1, and 0.25. CN, R, ΔE_0 and σ^2 denote the coordination number, inter-atomic distance, energy shift and Debye-Waller factor, respectively.[a].

Sample	Shell	CN (-)[b]	R (Å)	ΔE_0^c (eV)	σ^2 (Å^2)[d]	R-factor[e]
Sb−0.01	Sb-O	6.7 ± 1.0	1.98 ± 0.00	2.2 ± 1.2	0.004 ± 0.000	0.012
	Sb-Fe_1	4.0 ± 0.9	3.13 ± 0.01		0.004 ± 0.001	
	Sb-Fe_2	1.6 ± 0.7	4.03 ± 0.02		0.004 ± 0.001	
Sb−0.04	Sb-O	5.6 ± 0.6	1.99 ± 0.00	4.1 ± 0.7	0.003 ± 0.000	0.004
	Sb-Fe_1	5.5 ± 0.9	3.15 ± 0.01		0.007 ± 0.001	
	Sb-Fe_2	1.4 ± 0.6	3.99 ± 0.02		0.007 ± 0.001	
Sb−0.1	Sb-O	5.8 ± 0.7	1.99 ± 0.00	3.1 ± 1.0	0.003 ± 0.000	0.006
	Sb-Fe_1	3.1 ± 1.1	3.12 ± 0.01		0.008 ± 0.003	
	Sb-Fe_2	3.2 ± 1.1	3.57 ± 0.01		0.008 ± 0.003	
Sb−0.25	Sb-O	4.6 ± 0.6	1.98 ± 0.00	4.0 ± 1.10	0.002 ± 0.000	0.003
	Sb-Sb_1	1.9 ± 0.6	3.09 ± 0.02		0.002 ± 0.003	
	Sb-Fe_1	2.0 ± 1.0	3.14 ± 0.03		0.002 ± 0.002	
	Sb-Sb_2	2.7 ± 0.7	3.47 ± 0.03		0.002 ± 0.002	
	Sb-Fe_2	4.3 ± 1.4	3.53 ± 0.03		0.002 ± 0.002	

[a]Fit uncertainties are given for the last significant figure. [b]The amplitude reduction factor was set to 0.9 [62], and the uncertainty associated with this estimate has been included in the error of CN. [c]The energy shift was constrained to a single value for all shells for each spectrum. [d]For each spectrum, one fitted value for the Debye-Waller factor was allowed for near-neighbour oxygens, and another one for metal(loid) scatterers. [e] R-factor = $\Sigma_i(data_i\text{-}fit_i)^2/\Sigma_i\ data_i$.

that Sb(V) was retained by solids produced in the Sb-0.01 and Sb-0.04 treatment through incorporation into the lepidocrocite structure via Sb(V)-for-Fe(III) substitution. This finding agrees with the above-mentioned expansion of the lepidocrocite crystals along the b-axis, which was likely a consequence of the loss of H^+ from the lepidocrocite structure. The heterovalent substitution of Fe(III) by Sb(V) introduced additional positive charge into the lepidocrocite structure [59], which may have been compensated for by a release of H^+ ions. The incorporation of Sb(V) is thus likely to have weakened the hydrogen bonding between the $Fe(III)O_3OH_3$ layers, thereby leading to the observed increase in d-spacing from 6.3 to 8.3 Å (SI Figure S9, Table 1).

In agreement with the findings from the Sb-0.01 treatment, the Sb K-edge EXAFS data for solids produced in the Sb-0.1 treatment were also well described by two Sb-Fe paths (Table 3). The shorter of these two paths occurred at 3.12 Å, which is consistent with edge-sharing between SbO_6 and FeO_6 octahedra (as also found for the Sb-0.01 and Sb-0.04 treatments) [37,39,50]. The longer of the two Sb-Fe paths in the Sb-0.1 treatments was fit by an inter-atomic distance of 3.57 Å, which is consistent with double corner-sharing between adjacent SbO_6 and FeO_6 octahedra. This contrasts with the presence of single-corner sharing in the Sb-0.01 and Sb-0.04 treatments, but agrees with the XRD and Mössbauer spectroscopic results in that the local coordination environment in feroxyhyte is characterized by the presence of both edge and double-corner sharing linkages between FeO_6 octahedra [37,39]. This observation, together with relatively large CNs of ~3 for edge and double-corner sharing linkages between SbO_6 and FeO_6 in the Sb-0.1 treatment – compared with the expected CNs of 1–2 for adsorption complexes on the Fe(III) hydroxide surface – suggests that Sb(V) was retained within the feroxyhyte structure through Sb(V)-for-Fe(III) substitution [21,50].

Similar to the Sb-0.1 treatment, modelling of the Sb K-edge EXAFS data for the Sb-0.25 treatment also indicates the presence of two Sb-Fe paths (Table 3). These paths are characterized by inter-atomic distances of 3.14 Å and 3.52 Å with CNs of 2 and 4, respectively. As also observed for the Sb-0.1 treatment, these distances and CNs align with edge and double-corner sharing between SbO_6 and FeO_6 octahedra within the structure of the feroxyhyte that formed in the Sb-0.25 treatment. In addition to these Sb-Fe paths, solids produced in the Sb-0.25 treatment also contained additional Sb-Sb backscattering paths at inter-atomic distances of 3.09 Å and 3.47 Å (Table 3). The presence of Sb-Sb backscattering is supported by Morlet wavelet transform (WT) analysis for the 0.25 treatment, which (unlike the other treatments) shows a distinct feature at $k > 12$ Å^{-1} (SI Figure S2). The presence of these Sb-Sb paths, in addition to the more abundant Sb-Fe paths, likely reflects the relatively Sb-rich nature of the feroxyhyte that formed in the Sb-0.25 treatment (whereby this feroxyhyte was characterized by 16.2 mol% Sb(V)-for-Fe(III) substitution; Table 1).

Overall, the Sb K-edge EXAFS results show that Sb(V) was incorporated into the crystal structure of both lepidocrocite and feroxyhyte by heterovalent Sb(V)-for-Fe(III) substitution. Such substitution is feasible because Sb(V) and Fe(III) have comparable ion sizes (Sb(V): 0.60 Å; Fe(III): 0.55 Å) when octahedrally coordinated with O [6]. Substitution of Sb(V) into the structure of feroxyhyte has been previously described by Hockmann et al. [21] in a study examining the effect of Fe(II)-induced ferrihydrite transformation on Sb behavior. However, the present study provides direct evidence that Sb(V)-for-Fe(III) substitution can also occur in lepidocrocite. From the present results (Table 1), the upper limit for such substitution in lepidocrocite appears to be between 3.4 and 8.2 mol% (given lepidocrocite was the only Fe(III) phase present at 3.4 mol% substitution, whereas lepidocrocite was largely replaced by feroxyhyte at the higher 8.2 mol% substitution). At higher mol% levels, lepidocrocite formation was inhibited in favor of the formation of feroxyhyte, which can evidently accommodate larger degrees of Sb(V)-for-Fe(III) substitution (Table 1).

The results of the present study are of particular significance from an environmental pollution perspective as incorporation of Sb(V) into the crystal structure of Fe(III) hydroxide minerals may be a relatively secure immobilization mechanism for Sb(V) in Sb-contaminated environments. This is because incorporated Sb(V) species are expected to be largely protected from desorption that may induce changes in aqueous-phase properties such as pH, ionic strength, and competitive ions. To test this hypothesis, we subjected the Sb(V)-coprecipitated lepidocrocite and feroxyhyte from the Fe(II) oxidation experiments to extraction with a 1 M KH_2PO_4 solutions. The results show that only ~2 % to ~6 % of total solid phase Sb(V) was recovered by the 1 M KH_2PO_4 extraction (SI Figure S3), while ~75 % recovery would be expected if Sb(V) was surface-adsorbed (SI Section 3). Likewise, we also found that < 1 % of solid-phase Sb(V) was remobilized via the desorption assay described in the SI section. This very low recovery during both KH_2PO_4 extraction and the desorption assay support the concept that Sb(V) that is incorporated into the lepidocrocite or feroxyhyte structure is largely protected from short-term desorption processes.

4. Conclusion

This study has provided an in-depth systematic examination of the Fe(III) hydroxide mineral products and associated mechanisms of Sb(V) sequestration that result from near-neutral pH Fe(II) oxidation in the presence of Sb(V). The following key conclusions can be drawn from this study:

- Under our experimental conditions, oxidation of Fe(II) from solutions with molar Sb(V):Fe(II) ratios of less than 0.1 resulted in the formation of lepidocrocite. This is consistent with a large number of previous studies on Fe(II) oxidation in near-neutral pH environments.
- In contrast, at initial aqueous Sb(V):Fe(II) ratios greater than 0.1, oxidation of aqueous Fe(II) resulted in the formation of feroxyhyte. Although feroxyhyte is a relatively rare Fe(III) hydroxide in most surface environments, this finding suggests that it may occur more commonly in Sb(V)-rich waters that experience aqueous Fe(II) oxidation.
- The lepidocrocite and feroxyhyte that are formed via Fe(II) oxidation remove aqueous Sb(V) from solution by incorporating Sb(V) into their crystal structures via Sb(V)-for-Fe(III) substitution during mineral precipitation.
- The present study provides compelling evidence that lepidocrocite can retain Sb(V) via this heterovalent substitution mechanism (with our results suggesting that such substitution can occur at levels of up to somewhere between ~3.4 and ~8.2 mol%).
- Feroxyhyte that forms via Fe(II) oxidation can accommodate relatively large amounts of Sb(V)-for-Fe(III) substitution, with the highest level of substitution observed in the present study amounting to 16.2 mol%.
- Sb(V) that is incorporated into the structure of lepidocrocite and feroxyhyte appears to be largely protected from desorption processes, thereby suggesting formation of these Sb(V)-bearing Fe(III) hydroxides may securely immobilize Sb(V) in Sb-contaminated environments.

Even though this study lacks the complexity of natural systems, these findings expand our understanding of interactions between Sb geochemistry and the Earth's near-surface Fe cycle and emphasize the role that such interactions can play in controlling both Fe(III) hydroxide mineralogy and Sb mobility. Given, for example, that organic ligands can influence Fe(II) oxidation kinetics [61], and that co-occurring ions like arsenic may compete with Sb for binding sites during oxidation [45] or alter the properties of resulting precipitates [59], future research should build on these insights by investigating the impact of environmental matrices on Sb sequestration during Fe(II) oxidation.

Environmental implication

Antimony is a hazardous material, whose mobility in redox-dynamic environments may be controlled by interactions with Fe(III) hydroxide minerals that form via Fe(II) oxidation. This study examined the Fe(III) hydroxide mineral products and associated mechanisms of Sb(V) sequestration that result from Fe(II) oxidation in the presence of Sb(V). The outcomes enhance our fundamental understanding of Sb's environmental behavior by providing new insights into Sb(V) incorporation into Fe(III) hydroxides, while showing that such incorporation impacts the mineralogy of Fe(III) hydroxides that form via Fe(II) oxidation.

CRediT authorship contribution statement

Britta Planer-Friedrich: Writing – review & editing. **Stefan Peiffer**: Writing – review & editing. **Kerstin Hockmann**: Writing – review & editing, Supervision, Project administration, Methodology, Funding acquisition, Conceptualization. **Laura Wegner**: Writing – original draft, Investigation, Formal analysis, Data curation, Conceptualization. **Edward Burton**: Writing – review & editing, Supervision, Project administration, Funding acquisition, Conceptualization. **Catherine McCammon**: Writing – review & editing, Formal analysis. **Andreas C. Scheinost**: Writing – review & editing, Formal analysis.

Declaration of Competing Interest

The authors declare that they have no known competing financial interests or personal relationships that could have appeared to influence the work reported in this paper.

Acknowledgements

Funding from the Germany Academic Exchange Service (DAAD-PPP Australia grant no. 57446537), the Australian Research Council (grant no. FT200100449) and by the Female Professor Programme of Germany's Federal Ministry of Education and Research (BMBF), the Equal Opportunities Department at University of Bayreuth as well as the Heinrich Böll Foundation are gratefully acknowledged. We acknowledge the European Synchrotron Radiation Facility (ESRF) for provision of synchrotron radiation facilities and Dr. Graeme Auchterlonie for the collection of the TEM data at the University of Queensland, Australia. Laboratory assistance was given by Roz Hagan, Jutta Eckert, Martina Rohr, and Stefan Will. This research was supported by the Environmental Analysis Laboratory (EAL), which is a Southern Cross University NATA accredited research support facility.

Appendix A. Supporting information

Supplementary data associated with this article can be found in the online version at doi:10.1016/j.jhazmat.2025.137380.

Data availability

Data will be made available on request.

References

[1] APHA, 2017. Standard methods for the examination of water and wastewater, 23rd edition. ed. American Public Health Association, Washington, DC.
[2] Ashley, P.M., Craw, D., Graham, B.P., Chappell, D.A., 2003. Environmental mobility of antimony around mesothermal stibnite deposits, New South Wales, Australia and southern New Zealand. J Geochem Explor 77, 1–14. https://doi.org/10.1016/S0375-6742(02)00251-0.
[3] Ashley, P.M., Craw, D., Tighe, M.K., Wilson, N.J., 2006. Magnitudes, spatial scales and processes of environmental antimony mobility from orogenic gold–antimony mineral deposits, Australasia. Environ Geol 51, 499–507. https://doi.org/10.1007/s00254-006-0346-6.
[4] Bian, X., Dong, Y., Zhao, D., Ma, X., Qiu, M., Xu, J., et al., 2020. Microsized antimony as a stable anode in fluoroethylene carbonate containing electrolytes for rechargeable lithium-/sodium-ion batteries. ACS Appl Mater Interfaces 12, 3554–3562. https://doi.org/10.1021/acsami.9b18006.
[5] Birnie, A.C., Paterson, E., 1991. The mineralogy and morphology of iron and manganese oxides in an imperfectly-drained Scottish soil. Geoderma 50, 219–237. https://doi.org/10.1016/0016-7061(91)90036-S.
[6] Bolanz, R., Bläss, U., Ackermann, S., Ciobotă, V., Rösch, P., Tarcea, N., et al., 2013. The effect of antimonate, arsenate, and phosphate on the transformation of ferrihydrite to goethite, hematite, feroxyhyte, and tripuhyite. Clays Clay Miner 61, 11–25. https://doi.org/10.1346/CCMN.2013.0610102.
[7] Burton, E.D., Hockmann, K., Karimian, N., 2020. Antimony sorption to goethite: effects of Fe(II)-catalyzed recrystallization. ACS Earth Space Chem 4, 476–487. https://doi.org/10.1021/acsearthspacechem.0c00013.
[8] Burton, E.D., Hockmann, K., Karimian, N., Johnston, S.G., 2019. Antimony mobility in reducing environments: the effect of microbial iron(III)-reduction and associated secondary mineralization. GCA 245, 278–289. https://doi.org/10.1016/j.gca.2018.11.005.
[9] Burton, E.D., Karimian, N., Hamilton, J.L., Frierdich, A.J., 2022. Iron isotopes in acid mine drainage: extreme and divergent fractionation between solid (schwertmannite, jarosite, and ferric arsenate) and aqueous species. Environ Sci Technol 56, 18060–18068. https://doi.org/10.1021/acs.est.2c05999.
[10] Burton, E.D., Karimian, N., Johnston, S.G., Schoepfer, V.A., Choppala, G., Lamb, D., 2021. Arsenic-imposed effects on schwertmannite and jarosite formation in acid mine drainage and coupled impacts on arsenic mobility. ACS Earth Space Chem 5, 1418–1435. https://doi.org/10.1021/acsearthspacechem.1c00047.
[11] Cornell, R.M., Schwertmann, U., 2003. The Iron Oxides, 2nd, Completely Revised and Extended ed. ed. Wiley-VCH, Weinheim.
[12] Ferreira, H., S, C.M., Pinto, I.S., Soares, V., M, E., Soares, H.M.V., 2015. (Un) suitability of the use of pH buffers in biological, biochemical and environmental studies and their interaction with metal ions – a review. RSC Adv 5, 30989–31003. https://doi.org/10.1039/C4RA15453C.

[13] Filella, 2009. Natural attenuation processes applying to antimony: a study in the abandoned antimony mine in Goesdorf, Luxembourg. Sci Total Environ. https://doi.org/10.1016/j.scitotenv.2009.08.027.
[14] Filella, M., Belzile, N., Chen, Y.-W., 2002. Antimony in the environment: a review focused on natural waters. I Occur Earth Sci Rev 57, 125–176. https://doi.org/10.1016/S0012-8252(01)00070-8.
[15] Filella, M., Belzile, N., Chen, Y.-W., 2002. Antimony in the environment: a review focused on natural waters. II Relev Solut Chem Earth Sci Rev 59, 265–285. https://doi.org/10.1016/S0012-8252(02)00089-2.
[16] Filella, M., Hennebert, P., Okkenhaug, G., Turner, A., 2020. Occurrence and fate of antimony in plastics. J Hazard Mater 390, 121764. https://doi.org/10.1016/j.jhazmat.2019.121764.
[17] Filella, M., Williams, P.A., Belzile, N., 2009. Antimony in the environment: knowns and unknowns. Environ Chem 6, 95. https://doi.org/10.1071/EN09007.
[18] Funke, 2005. Wavelet analysis of extended X-ray absorption fine structure data. Phys. Rev. B. https://doi.org/10.1103/PhysRevB.71.094110.
[19] Gemici, Ü., Tarcan, G., 2007. Assessment of the pollutants in farming soils and waters around untreated abandoned Türkönü mercury mine (Turkey). Bull Environ Contam Toxicol 79, 20–24. https://doi.org/10.1007/s00128-007-9087-9.
[20] He, M., Wang, N., Long, X., Zhang, C., Ma, C., Zhong, Q., et al., 2019. Antimony speciation in the environment: Recent advances in understanding the biogeochemical processes and ecological effects. J Environ Sci 75, 14–39. https://doi.org/10.1016/j.jes.2018.05.023.
[21] Hockmann, K., Karimian, N., Schlagenhauff, S., Planer-Friedrich, B., Burton, E.D., 2021. Impact of antimony(V) on iron(II)-catalyzed ferrihydrite transformation pathways: a novel mineral switch for feroxyhyte formation. Environ Sci Technol. https://doi.org/10.1021/acs.est.0c08660.
[22] Hockmann, K., Lenz, M., Tandy, S., Nachtegaal, M., Janousch, M., Schulin, R., 2014. Release of antimony from contaminated soil induced by redox changes. J Hazard Mater 275, 215–221. https://doi.org/10.1016/j.jhazmat.2014.04.065.
[23] Hockmann, K., Planer-Friedrich, B., Johnston, S.G., Peiffer, S., Burton, E.D., 2020. Antimony mobility in sulfidic systems: coupling with sulfide-induced iron oxide transformations. Geochim Et Cosmochim Acta 282, 276–296. https://doi.org/10.1016/j.gca.2020.05.024.
[24] Hosseinpour Moghaddam, M., Karimian, N., Johnston, S.G., Choppala, G., Rastegari, M., Burton, E.D., 2024. Antimony(V) sorption and coprecipitation with ferrihydrite: an examination of retention mechanisms and the selectivity of commonly-applied extraction procedures. J Hazard Mater 480, 136297. https://doi.org/10.1016/j.jhazmat.2024.136297.
[25] Huggins, F.E., Huffman, G.P., Lin, M.C., 1983. Observations on low-temperature oxidation of minerals in bituminous coals. Int J Coal Geol 3, 157–182. https://doi.org/10.1016/0166-5162(83)90008-3.
[26] Jia, S., Zhu, Q., Wu, H., Chu, M., Han, S., Feng, R., et al., 2020. Efficient electrocatalytic reduction of carbon dioxide to ethylene on copper–antimony bimetallic alloy catalyst. Chin J Catal 41, 1091–1098. https://doi.org/10.1016/S1872-2067(20)63542-2.
[27] Johnston, S.G., Bennett, W.W., Doriean, N., Hockmann, K., Karimian, N., Burton, E.D., 2020. Antimony and arsenic speciation, redox-cycling and contrasting mobility in a mining-impacted river system. Sci Total Environ 710, 136354. https://doi.org/10.1016/j.scitotenv.2019.136354.
[28] Kandegedara, A., Rorabacher, D.B., 1999. Noncomplexing tertiary amines as "better" buffers covering the range of pH 3−11. Temperature dependence of their acid dissociation constants. Anal Chem 71, 3140–3144. https://doi.org/10.1021/ac9902594.
[29] Karimian, N., Johnston, S.G., Burton, E.D., 2017. Antimony and arsenic behavior during Fe(II)-induced transformation of jarosite. Environ Sci Technol 51, 4259–4268. https://doi.org/10.1021/acs.est.6b05335.
[30] Keon, N.E., Swartz, C.H., Brabander, D.J., Harvey, C., Hemond, H.F., 2001. Validation of an arsenic sequential extraction method for evaluating mobility in sediments. Environ Sci Technol 35, 2778–2784. https://doi.org/10.1021/es001511o.
[31] Kirsch, R., Fellhauer, D., Altmaier, M., Neck, V., Rossberg, A., Fanghänel, T., et al., 2011. Oxidation State and Local Structure of Plutonium Reacted with Magnetite, Mackinawite, and Chukanovite. Environ Sci Technol 45, 7267–7274. https://doi.org/10.1021/es200645a.
[32] Lagarec, K., Rancourt, D., 1998. Recoil − Mössbauer spectral analysis software for Windows.
[33] Leuz, A.-K., Mönch, H., Johnson, C.A., 2006. Sorption of Sb(III) and Sb(V) to goethite: influence on Sb(III) oxidation and mobilization. Environ Sci Technol 40, 7277–7282. https://doi.org/10.1021/es061284b.
[34] Li, X., Graham, N.J.D., Deng, W., Liu, M., Liu, T., Yu, W., 2022. Structural variation of precipitates formed by Fe(II) oxidation and impact on the retention of phosphate. Environ Sci Technol 56, 4345–4355. https://doi.org/10.1021/acs.est.1c06256.
[35] Liang, S., Cheng, Y., Zhu, J., Xia, Y., Müller-Buschbaum, P., 2020. A chronicle review of nonsilicon (Sn, Sb, Ge)-based lithium/sodium-ion battery alloying anodes. Small Methods 4, 2000218. https://doi.org/10.1002/smtd.202000218.
[36] Lucas, F.W.S., Lima, F.H.B., 2020. Electrodeposited tin-antimony alloys as novel electrocatalysts for selective and stable carbon dioxide reduction to formate. ChemElectroChem 7, 3733–3742. https://doi.org/10.1002/celc.202000769.
[37] Manceau, A., Drits, V.A., 1993. Local structure of ferrihydrite and feroxyhite by exafs spectroscopy. Clay Min 28, 165–184. https://doi.org/10.1180/claymin.1993.028.2.01.
[38] Mitsunobu, S., Harada, T., Takahashi, Y., 2006. Comparison of antimony behavior with that of arsenic under various soil redox conditions. Environ Sci Technol 40, 7270–7276. https://doi.org/10.1021/es060694x.
[39] Mitsunobu, S., Takahashi, Y., Terada, Y., Sakata, M., 2010. Antimony(V) incorporation into synthetic ferrihydrite, goethite, and natural iron oxyhydroxides. Environ Sci Technol 44, 3712–3718. https://doi.org/10.1021/es903901e.
[40] Murad, E., 2013. Mössbauer spectroscopy. Dev Clay Sci 5, 11–24. https://doi.org/10.1016/B978-0-08-098259-5.00003-2.
[41] Okkenhaug, G., Zhu, Y.-G., He, J., Li, X., Luo, L., Mulder, J., 2012. Antimony (Sb) and arsenic (As) in Sb mining impacted paddy soil from Xikuangshan, China: differences in mechanisms controlling soil sequestration and uptake in rice. Environ Sci Technol 46, 3155–3162. https://doi.org/10.1021/es2022472.
[42] Ondrejková, I., Ženišová, Z., Fľaková, R., Krčmář, D., Sracek, O., 2013. The distribution of antimony and arsenic in waters of the dúbrava abandoned mine site, slovak republic. Mine Water Environ 32, 207–221. https://doi.org/10.1007/s10230-013-0229-5.
[43] Patrat, G., Bergevin, F., Pernet, M., Joubert, J.C., 1983. Structure locale de δ-FeOOH. Acta Crystallogr Sect B Struct Sci 39, 165–170. https://doi.org/10.1107/S0108768183002232.
[44] Prescher, C., McCammon, C., Dubrovinsky, L., 2012. MossA: a program for analyzing energy-domain Mössbauer spectra from conventional and synchrotron sources. J Appl Cryst 45, 329–331. https://doi.org/10.1107/S0021889812004979.
[45] Qi, P., Pichler, T., 2017. Competitive adsorption of As(III), As(V), Sb(III) and Sb(V) onto ferrihydrite in multi-component systems: Implications for mobility and distribution. J Hazard Mater 330, 142–148. https://doi.org/10.1016/j.jhazmat.2017.02.016.
[46] Radková, A., Jamieson, H.E., Campbell, K.M., 2020. Antimony mobility during the early stages of stibnite weathering in tailings at the Beaver Brook Sb deposit, Newfoundland. Appl Geochem 115, 104528. https://doi.org/10.1016/J.APGEOCHEM.2020.104528.
[47] Rastegari, M., Karimian, N., Johnston, S.G., Doherty, S.J., Hamilton, J.L., Choppala, G., et al., 2022. Antimony(V) incorporation into schwertmannite: critical insights on antimony retention in acidic environments. Environ Sci Technol 56, 17776–17784. https://doi.org/10.1021/acs.est.2c07341.
[48] Ravel, B., Newville, M., 2005. ATHENA, ARTEMIS, HEPHAESTUS: data analysis for X-ray absorption spectroscopy using IFEFFIT. J Synchrotron Rad 12, 537–541. https://doi.org/10.1107/S0909049505012719.
[49] Scheinost, A.C., Claussner, J., Exner, J., Feig, M., Findeisen, S., Hennig, C., et al., 2021. ROBL-II at ESRF: a synchrotron toolbox for actinide research. J Synchrotron Radiat 28, 333–349. https://doi.org/10.1107/S1600577520014265.
[50] Scheinost, A.C., Rossberg, A., Vantelon, D., Xifra, I., Kretzschmar, R., Leuz, A.-K., et al., 2006. Quantitative antimony speciation in shooting-range soils by EXAFS spectroscopy. Geochim Et Cosmochim Acta 70, 3299–3312. https://doi.org/10.1016/j.gca.2006.03.020.
[51] Schwertmann, U., Cornell, R.M., 2000. Iron oxides in the laboratory, 2., completely rev. and extended ed. ed. Wiley-VCH, Weinheim. https://doi.org/10.1002/9783527613229.
[52] Senn, A.-C., Kaegi, R., Hug, S.J., Hering, J.G., Mangold, S., Voegelin, A., 2015. Composition and structure of Fe(III)-precipitates formed by Fe(II) oxidation in water at near-neutral pH: Interdependent effects of phosphate, silicate and Ca. Geochim Et Cosmochim Acta 162, 220–246. https://doi.org/10.1016/j.gca.2015.04.032.
[53] Sher Shah, M.S.A., Oh, C., Park, H., Hwang, Y.J., Ma, M., Park, J.H., 2020. Catalytic oxidation of methane to oxygenated products: recent advancements and prospects for electrocatalytic and photocatalytic conversion at low temperatures. Adv Sci 7, 2001946. https://doi.org/10.1002/advs.202001946.
[54] U.S. Geological Survey, (2020). Mineral commodity summaries 2020. U.S. Geological Survey; 200 p, 10.3133/mcs2020.
[55] United Nations Environmental Program, 2019. Basel Convention on the Control of Transboundary Movements of Hazardous Wastes and Their Disposal (Text and Annexes, Revised in 2019).
[56] United States Environmental Protection Agency, 2009. National Primary Drinking Water Regulations. EPA 816-F-09-004.
[57] Vodyanitskii, Yu.N., 2009. Mineralogy and geochemistry of manganese: a review of publications. Eurasia Soil Sc 42, 1170–1178. https://doi.org/10.1134/S1064229309100123.
[58] Vodyanitskii, Yu.N., 2010. Iron hydroxides in soils: a review of publications. Eurasia Soil Sci 43, 1244–1254. https://doi.org/10.1134/S1064229310110074.
[59] Wang, W., He, M., Lin, C., Ouyang, W., Liu, X., 2024. Unveiling the influence of antimony substitution on the surface properties and adsorption behavior of ferrihydrite: from molecular mechanisms to environmental implications. Environ Sci Technol 58, 14475–14485. https://doi.org/10.1021/acs.est.4c02726.
[60] Wang, Y., He, M., Lin, C., Ouyang, W., Liu, X., 2024. Novel insights into Sb(III) oxidation and immobilization during ferrous iron oxygenation: the overlooked roles of singlet oxygen and Fe (oxyhydr)oxides formation. Environ Sci Technol. https://doi.org/10.1021/acs.est.4c02006.
[61] Wang, Y., Kong, L., He, M., Lin, C., Ouyang, W., Liu, X., et al., 2023. Mechanistic insights into Sb(III) and Fe(II) co-oxidation by oxygen and hydrogen peroxide: dominant reactive oxygen species and roles of organic ligands. Water Res 242, 120296. https://doi.org/10.1016/j.watres.2023.120296.
[62] Yan, L., Chan, T., Jing, C., 2022. Mechanistic study for antimony adsorption and precipitation on hematite facets. Environ Sci Technol 56, 3138–3146. https://doi.org/10.1021/acs.est.1c07801.